ACS Photonics

pubs.acs.org/journal/apchd5

Article

Quasi-CW Lasing from Directly Patterned and Encapsulated Perovskite Cavity at 260 K

Jiyoung Moon,[○] Masoud Alahbakhshi,[○] Abouzar Gharajeh,[○] Quanwei Li, Zhitong Li, Ross Haroldson, Sunah Kwon, Roberta Hawkins, Moon J. Kim, Walter Hu, Xiang Zhang, Anvar Zakhidov, and Qing Gu*

Cite This: *ACS Photonics* 2022, 9, 1984–1991

Read Online

ACCESS | Metrics & More | Article Recommendations | Supporting Information

ABSTRACT: Metal halide perovskites have emerged as promising gain materials for on-chip lasers in photonic integrated circuits. For these to become commercially relevant as economical on-chip light sources, a clear onset of quasi-continuous wave (quasi-CW) and, eventually, continuous wave (CW) lasing at room temperature or Peltier-cooling accessible temperatures from directly patterned perovskite cavities is a critical milestone that must be achieved. Herein, through directly patterning with nanoimprint lithography and encapsulation of the cavity with a thin layer of polycarbonate (PC), quasi-CW lasing from $CH_3NH_3PbBr_3$ ($MAPbBr_3$) is demonstrated up to 260 K. The PC layer is also shown to effectively encapsulate the surface defects of $MAPbBr_3$ and protect devices from environmental hazards. Through the combined analysis of the crystal quality, degradation process during optical pumping, defect encapsulation, and laser performance, room temperature CW lasing from directly patterned perovskite cavities should be within reach.

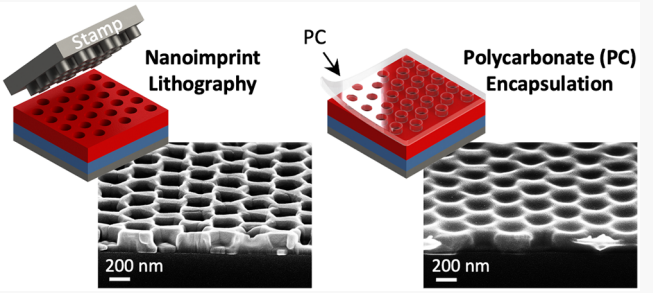

KEYWORDS: *$CH_3NH_3PbBr_3$, polycarbonate, nanoimprint lithography, on-chip light source, photonic crystal laser*

INTRODUCTION

An economical on-chip light source is a crucial component in high-performance photonic integrated circuits (ICs).[1−4] Although inorganic III−V and III−Nitride semiconductor lasers can be highly efficient and stable, they are typically off-chip due to the difficulty of their integration with the silicon (Si) platform. Consequently, the system suffers from large coupling loss between the off-chip light source and Si chip at a high packaging expense. Coupling loss and packaging cost reductions have been reported for heterogeneously integrated lasers on Si via wafer bonding[1,3] and homogeneously integrated III−V lasers on Si.[4] In the quest for alternative gain media for cost-effective and Si-compatible on-chip lasers, solution-processed and widely tunable metal halide perovskites have been recognized as a promising candidate since the first demonstration of the perovskite laser in 2014.[5−21] In particular, hybrid organic−inorganic lead halide perovskites ($MAPbX_3$; MA = $CH_3NH_3^+$, X = Br^-, I^-, Cl^-) have shown remarkably low lasing thresholds, where lasing action is ascribed to a correlated electron−hole plasma.[7,8] Moreover, perovskites hold great promise for optoelectronic devices beyond lasers[22] because of their high quantum efficiency, balanced ambipolar charge transfer, strong light absorption, and long carrier lifetime.[23−26] However, an electrically pumped perovskite laser—a major goal of perovskite laser research—has not yet been demonstrated. Optically pumped lasing under continuous wave (CW) excitation without any substrate cooling is a crucial intermediate step to achieve this goal. Although a number of CW perovskite lasers have been reported, only a handful of them show a clear indication of the onset of lasing from the light−light (LL) curve and spectral evolution.[9,10] The optical cavities in these reports are formed by spin-coating a perovskite thin film on prepatterned substrates, which lacks dimension control and repeatability. However, to insert perovskite lasers into photonic ICs in a manufacturing friendly manner, directly patterned perovskite cavities with improved fabrication repeatability, high throughput yield, dimension controllability, and a smooth surface are desired. To this end, a few directly patterned perovskite lasers have been reported, but all were tested under optical pumping with pulses of 100 fs to 5 ns in the effective pulsed regime (when the pulse width is shorter than perovskite's carrier lifetime).[11−16] In fact, we previously reported CW lasing at room temperature (RT) from a directly patterned $MAPbI_3$-distributed feedback cavity, which lacks a clear indication of the onset of lasing.[27] Through ongoing research, we discovered that CW lasing was not actually achieved because of the

Received: January 13, 2022
Published: May 25, 2022

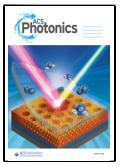

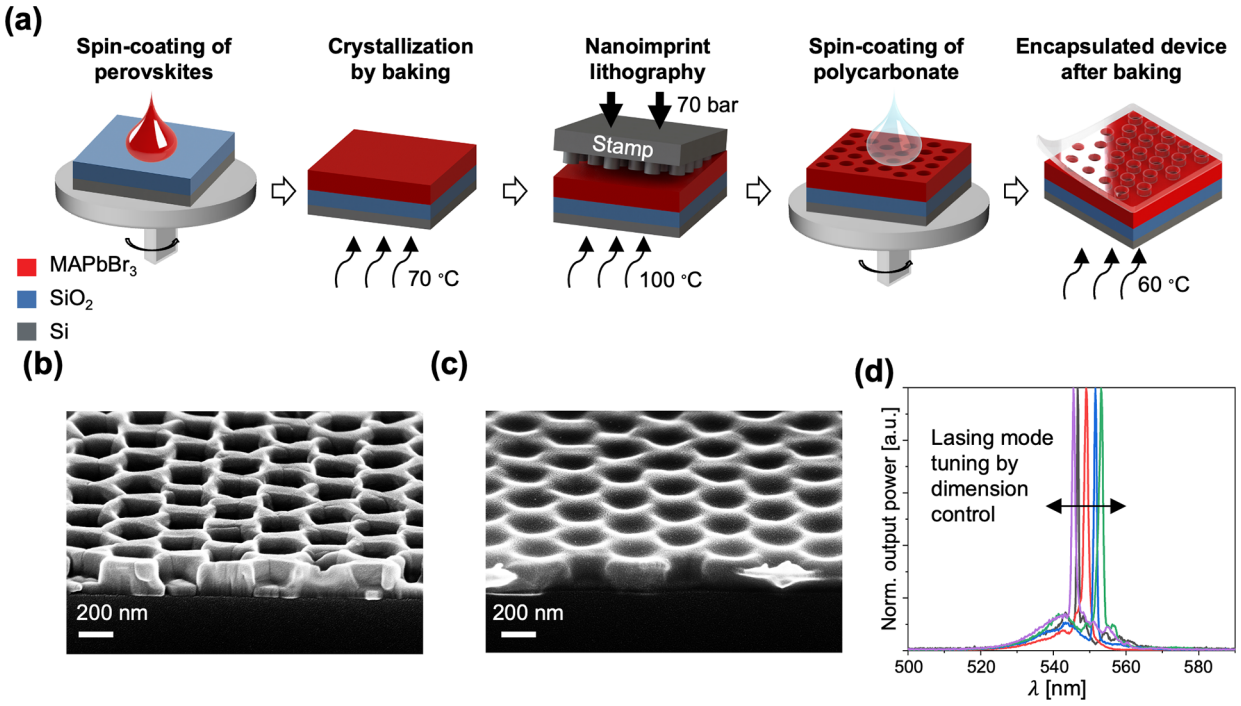

Figure 1. (a) Schematic of key fabrication steps. SEM images of the nanoimprinted $MAPbBr_3$ 2D PhC laser (b) before and (c) after PC encapsulation. (d) Lasing mode tuning by PhC dimension control at 200 K.

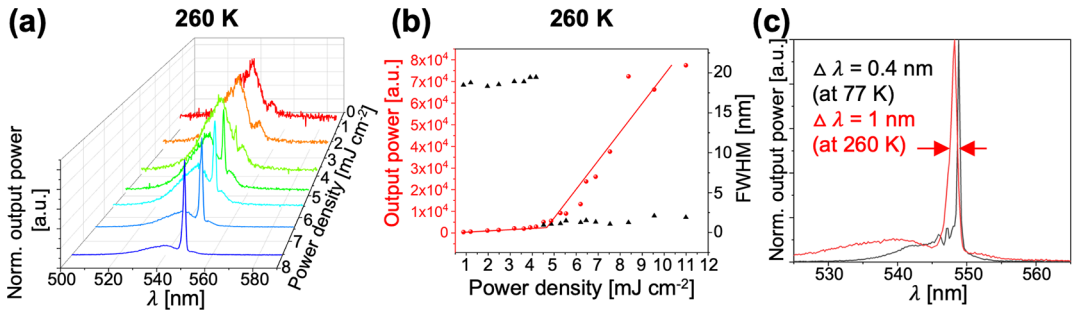

Figure 2. (a) Evolution of the emission spectra. (b) Integrated output power and fwhm as a function of pump power density. (c) Emission spectra of the laser showing a lasing wavelength blue-shift and widening of the line width from 77 K ($1.52 \times P_{th}$) to 260 K ($1.67 \times P_{th}$).

absence of a line width narrowing at the threshold, and the narrow emission line that was present at low pump powers below the reported threshold likely originated from a modified spontaneous emission effect.[28] A demonstration of quasi-CW (e.g., when the pulse width of the excitation source is longer than the carrier lifetime of the material) and, eventually, CW lasing at RT or Peltier-cooling accessible temperatures from directly patterned perovskite cavities with a smooth surface is required for perovskite lasers to be commercially relevant as economical on-chip light sources.

In this work, we unambiguously show quasi-CW lasing from directly patterned and encapsulated $MAPbBr_3$ photonic crystal (PhC) cavities up to 260 K. Because the carrier lifetime of polycrystalline $MAPbBr_3$ is shorter than 10 ns,[29−31] the quasi-CW pumping condition is satisfied when the optical excitation duration is longer than 10 ns. In our case, optical pulses of 17 ns duration and 355 nm wavelength are used as the quasi-CW pump source. The PhC laser cavity is directly patterned using the manufacturing-friendly thermal nanoimprint lithography (NIL) and subsequently encapsulated with a thin layer of polycarbonate (PC). With the operation occurring within a Peltier-cooling accessible temperature range, this work paves a path toward CW lasing in directly patterned perovskite cavities. In addition, it provides insights into the degradation process of $MAPbBr_3$ during optical pumping and presents a novel method to encapsulate perovskite effectively with negligible effect on the lasing threshold.

RESULTS

The first step toward a high-quality laser cavity composed of perovskite thin film gain medium is the development of a well-controlled direct patterning method for perovskite. Our approach is to use the manufacturing-friendly NIL with customized SiO_2 stamps. The height of the stamp is chosen to be 140 nm to efficiently confine the fundamental mode while minimizing the number of modes in the vertical direction. Next, perovskite residue thickness, nanohole diameter, and PhC period are varied to tune the fundamental mode wavelength to the center of the gain spectrum for $MAPbBr_3$. The stamps are fabricated by electron-beam (e-beam) lithography to have a PhC period of 315−365 nm, a diameter of 200−280 nm, and a height of 140 nm (stamp

https://doi.org/10.1021/acsphotonics.2c00071
ACS Photonics 2022, 9, 1984−1991

fabrication method and pattern map are shown in section 2 of Supplementary Part A). As depicted in Figure 1a, $MAPbBr_3$ films are first spin-coated on SiO_2 (1 μm) on Si substrates and crystallized by annealing at 70 °C for 5 min. Next, NIL is performed on the thin film at 100 °C and 70 bar pressure for 20 min to create a $MAPbBr_3$ 2D PhC cavity, which is subsequently encapsulated with a thin layer of PC. Further fabrication details of PC-encapsulated 2D PhCs are described in section 1 ($MAPbBr_3$ thin film fabrication), section 3 (nanoimprint lithography), and section 4 (PC formation) of Supplementary Part A. Figure 1 panels b and c show the scanning electron microscopy (SEM) images of the $MAPbBr_3$ cavity before and after PC encapsulation, respectively. Figure 1c shows that 50 nm of PC uniformly coats the $MAPbBr_3$ PhC. As shown in Figure 1d, the lasing mode wavelength can be tuned over a wide range by tuning the PhC cavity dimension. This can be accomplished either by changing the dimension of the NIL stamp or by changing the perovskite residue thickness with the same NIL stamp, which changes the cavity's effective permittivity. Increasing both the thickness of the PC layer and perovskite residue layer increases the effective permittivity of the material stack, leading to a red-shifted lasing wavelength. Conversely, increasing the nanohole diameter decreases the effective permittivity, leading to a blue-shifted lasing wavelength. This trend is also supported by the simulation result in Figure S6.

Figure 2 panels a and b present the spectral evolution and light-in versus light-out characteristics of the encapsulated $MAPbBr_3$ PhC laser at 260 K, respectively. At low pump power densities, a narrower and enhanced asymmetric photoluminescence (PL) spectrum compared with the PL from outside of the pattern (i.e., thin film PL) is observed because of the spectral filtering by the periodicity of PhC.[32,33] The intensity from the asymmetric PL increases with pump energy density up to 1.96 mJ cm^{-2} (0.435 × $P_{th}^{260\ K}$) and remains almost constant at ≥2.48 mJ cm^{-2} (0.55 × $P_{th}^{260\ K}$). At 3.9 mJ cm^{-2} (0.86 × $P_{th}^{260\ K}$), a sharp peak appears at ∼548 nm. With increasing pump power, the side-mode suppression ratio (SMSR) of the mode rapidly increases to 1.27 dB, resulting in a kink in the LL curve at ∼4.5 mJ cm^{-2}. The fwhm evolution in Figure 2b shows the expected sudden narrowing of the mode line width to 0.9 nm at 4.5 mJ cm^{-2}, which signifies the onset of lasing. With further increasing pump power, the SMSR continuously increases and reaches a maximum of 11.77 dB at 8.37 mJ cm^{-2}. We note that, at above the threshold, the fwhm fluctuates with an increasing trend, which can be attributed to the interplay between the temperature-dependent exciton−phonon interaction and the pump-power dependent gain coefficient.[14] Figure 2c shows the lasing line width of 1 nm at 1.67 × $P_{th}^{260\ K}$ and a much narrower lasing line width of 0.4 nm from the same pattern when tested at 77 K at 1.52 × P_{th}^{77K} for comparison.

Temperature-dependent lasing behavior is depicted in Figure 3. As temperature rises, the lasing threshold gradually increases, with a 15× difference between 77 and 260 K. Figure S7 summarizes the lasing threshold's dependence on temperature. Note that the pump laser's repetition rate is 100 kHz for 77−200 K, but a 10 kHz repetition rate is employed for 230 and 260 K to reduce self-heating, which may be a reason why the slope efficiency at 230 K is slightly higher than that at 200 K. If 10 kHz was used for all temperatures, the lasing threshold of 77−200 K would be lower than those reported. Nonetheless, the trend of an increasing threshold with increasing temperature is still observed.

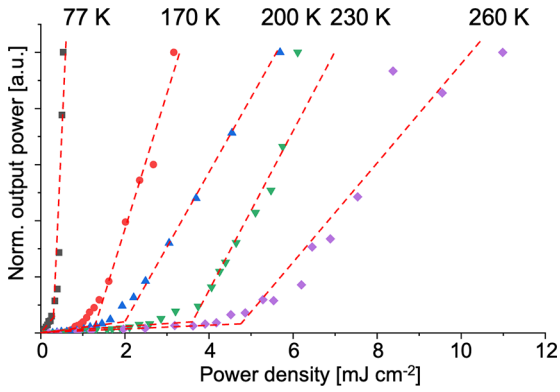

Figure 3. Normalized integrated output power as a function of pump power density at different temperatures.

The increase in the lasing threshold can be attributed to the increased loss and decreased optical gain with increasing temperature.[34,35] We note that reduction of gain with increasing temperature is the general trend in semiconductor gain materials.[36,37] However, in contrast to conventional semiconductors, such as III−V, in which the emission wavelength red-shifts as temperature increases,[36,38] the emission wavelength of $MAPbBr_3$ blue-shifts with increasing temperature, as shown in Figure 2c and Figure S8a. This is attributed to the phase transition of $MAPbBr_3$ with increasing temperature, namely, from orthorhombic to tetragonal phase at 130−150 K and from tetragonal to cubic phase at 230−250 K.[29]

Figure 4a,b shows the cavity dimension's effects on lasing performance at 260 K. For the device with the desired cavity dimensions of diameter of 205 nm, period of 315 nm, depth of 140 nm, PC thickness of 50 nm, and perovskite residue thickness of 11 nm (Figure 4a) where we design the highest Q mode to be at the thin film waveguide resonance (see the distribution of simulated cavity modes in Figure S6a), the lasing mode at 548 nm is the dominant cavity mode

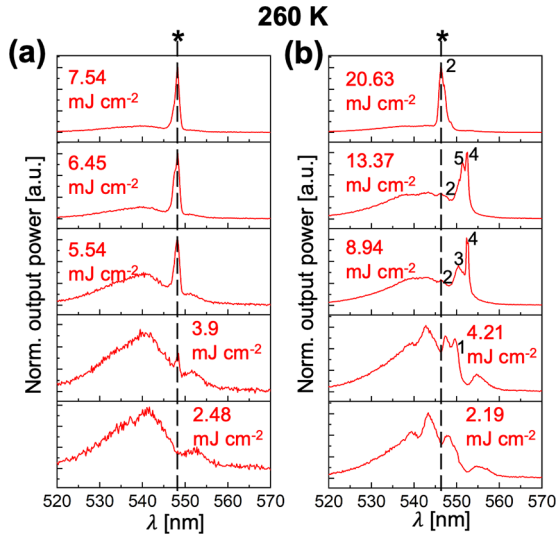

Figure 4. Evolution of the emission spectra from the laser with (a) desired and (b) undesired dimensions showing multiple modes marked by numbers at 260 K. * = lasing mode.

https://doi.org/10.1021/acsphotonics.2c00071
ACS Photonics 2022, 9, 1984−1991

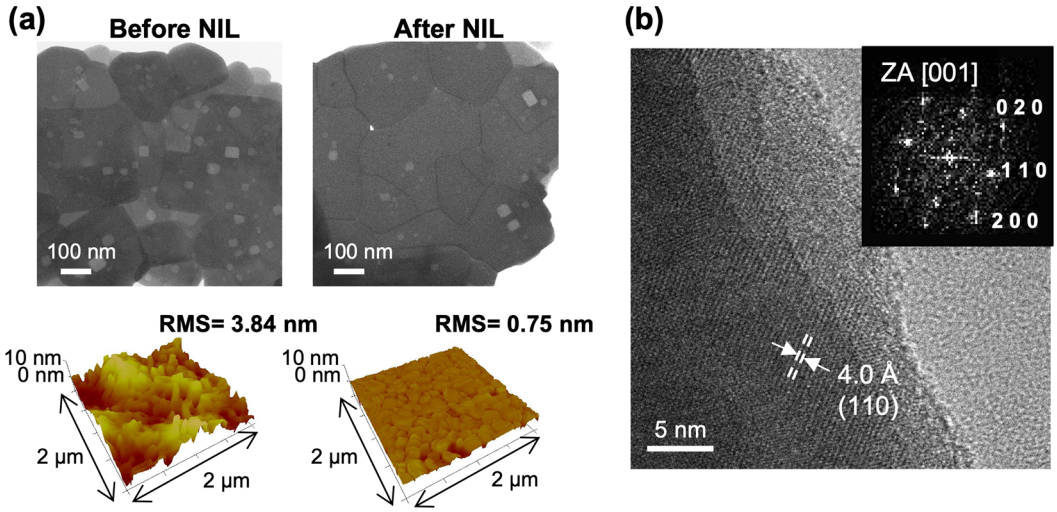

Figure 5. (a) STEM (top) and AFM (bottom) of $MAPbBr_3$ thin film before (left) and after (right) NIL. (b) TEM of $MAPbBr_3$ thin film after NIL (inset: FFT pattern with [001] zone axis).

throughout the entire pumping power range. This mode has a low threshold because it is at both the PhC band-edge resonance and the thin film waveguide resonance that is directly related to the optical gain of a material without requiring additional optical feedback.[39,40] Figure S8b shows the amplified spontaneous emission (ASE) from $MAPbBr_3$ thin film's waveguide resonance (measured outside of the patterned PhC area) at various temperatures to be 10 mJ cm^{-2} ($\cong 2.2 \times P_{th}^{260\ K}$), in which clear ASE at 548−549 nm can be seen at temperatures below 230 K (see Supplementary Part E for the details of the optical characteristics of imprinted $MAPbBr_3$ thin films).

However, multiple modes are observed at low pump powers in a device with undesired cavity dimensions of diameter of 240 nm, period of 325 nm, depth of 140 nm, PC thickness of 50 nm, and perovskite residue thickness of 37 nm, marked by numbers in Figure 4b. These modes include mode #1 at 549.61 nm, mode #2 at 546.3 nm, mode #3 at 550.39 nm, and mode #4 at at 552.3 nm. At high pump powers, the mode #2 at 546.3 nm wins the mode competition and becomes the lasing mode. However, the lasing threshold of this device is 2 times higher than that with the desired dimensions due to poor overlap between the high Q mode and perovskite gain.

Because perovskite thin film quality and device performance are intrinsically intertwined, improvements on a perovskite's morphological properties such as enlargement of grain size,[41,42] surface-passivation,[43,44] and an increase of the preferred crystal orientation[41] all lead to improved device performance. We show that the imprinted $MAPbBr_3$ has excellent morphology and crystallinity and that PC encapsulation on the imprinted film leads to an enhanced stability because PC not only blocks environmental hazards but also improves the surface quality of $MAPbBr_3$ film by encapsulating the defects.

Thanks to the surface-energy-driven grain growth of perovskites during NIL,[41] the grain size of $MAPbBr_3$ is enlarged, and the number of pinholes is reduced. We note that a flat stamp is used for NIL effect study. The scanning transmission electron microscopy (STEM) images in Figure 5a show that, after NIL, the number crystallographically controlled voids, indicated by the bright regions, decreases by ∼65%. SEM study also confirms the morphology improvement with a reduced number of voids, a smoother surface, and increased grain size (see Figure S9a,b for SEM images of $MAPbBr_3$ thin films before and after NIL, respectively). The surface roughness reduction is quantified by atomic force microscopy (AFM), as depicted in Figure 5a (bottom images). Before NIL, the film has a root-mean-square (RMS) roughness of 3.84 nm from a 2 × 2 μm area. After NIL, the RMS roughness is reduced by 5-fold, to 0.75 nm.

We directly observe the crystallinity and crystal structure of $MAPbBr_3$ after NIL by carrying out high-resolution TEM (HRTEM) measurements, which require a specimen with a relatively flat/smooth surface. In the case of a perovskite, TEM measurements are challenging for two main reasons. First, the typical process of making TEM specimens (e.g., Focused Ion Beam (FIB) for thinning down the material) damages a perovskite, introducing artifacts in the image. Second, the crystallinity of perovskite grains gets destroyed by e-beam energy within seconds, as shown in Figure S12. Therefore, to obtain TEM images on an e-beam-sensitive perovskite, quick focusing of the beam and quick imaging are necessary. For $MAPbBr_3$ thin films before NIL, meaningful TEM images cannot be obtained because of the rough surface of the film, as shown in Figure S13. In contrast, films after NIL show clearly observable periodic arrays of atoms in Figure 5b, owing to the smooth surface (RMS = 0.75 nm) that results from NIL. An interplanar spacing of 4 Å indexable to the (110) planes of a cubic structure is observed. The inset of Figure 5b shows the fast Fourier transform (FFT) pattern with the [001] zone axis of $MAPbBr_3$. Such direct observation of the arrangement of atoms allows us to conclude that the $MAPbBr_3$ film after NIL contains highly crystalline structures.

Although NIL enhances the film quality and, thus, the optical property (Figure S9c), the imprinted $MAPbBr_3$ still contains defects and grain boundaries that serve as trigger points of degradation. We further improve the device quality by encapsulating the trigger points with a thin layer of PC film. Compared with the popular choice of encapsulation by grown Al_2O_3 atomic layer deposition (ALD),[45−48] we find PC encapsulation to be more suitable because of its better uniformity, lower processing temperature, cost-effectiveness, and fabrication simplicity. The surface of PC-encapsulated $MAPbBr_3$ films is smoother and contains less defects than those encapsulated by ALD-Al_2O_3 (see section 2 of

https://doi.org/10.1021/acsphotonics.2c00071
ACS Photonics 2022, 9, 1984−1991

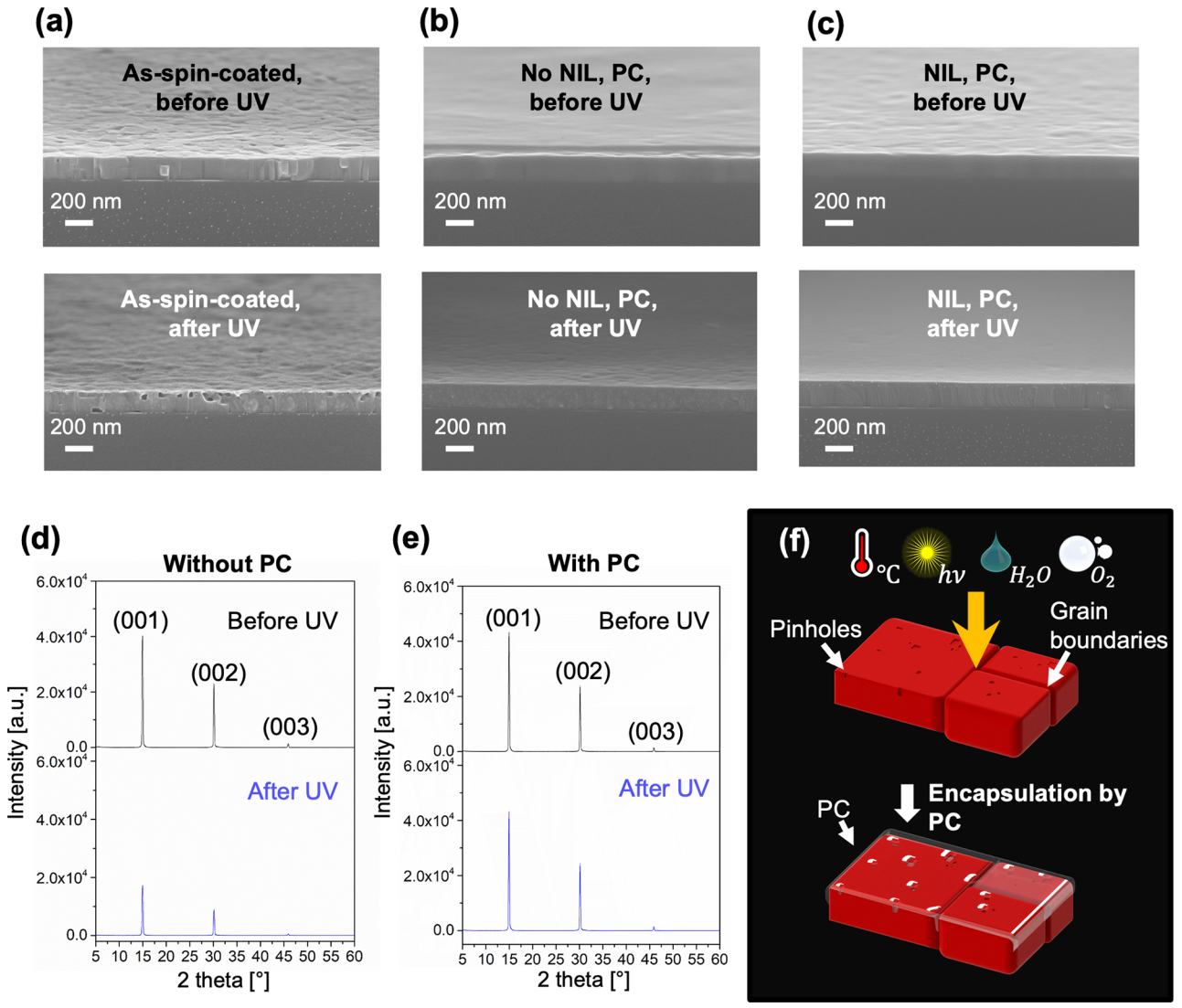

Figure 6. SEM images of (a) as-spin-coated film, (b) PC-encapsulated $MAPbBr_3$, and (c) PC-encapsulated $MAPbBr_3$ with NIL before (top) and after (bottom) UV. XRD spectra showing the effect of UV exposure on $MAPbBr_3$ film (d) without and (e) with PC encapsulation, before (top) and after (bottom) UV. (f) Schematic of PC encapsulation to prevent perovskite degradation from heat, photon energy from UV, moisture, and oxygen.

Supplementary Part F for the study of encapsulation with ALD-Al_2O_3).

We find photoinduced damage in the $MAPbBr_3$ PhC laser without any encapsulation after testing with optical pumping, in which destroyed the PhC structure can be seen (Figure S10c). We treat the PC-encapsulated $MAPbBr_3$ thin films with more extreme conditions than our typical optical pumping condition to better show the effect of PC encapsulation, especially during laser operation far above the lasing threshold. We illuminate the film with high photon energies of 4.8 and 6.7 eV using a low-pressure mercury lamp without any substrate cooling in atmosphere.

Figure 6a shows that without PC's protection, UV light destroys perovskite grains. Compared with the as-spin-coated film in Figure 6a (top), more pinholes and a roughened surface are evident after UV exposure (Figure 6a-bottom). Conversely, once encapsulated with PC, perovskite grains are protected from UV [Figure 6b (top) in comparison with Figure 6b (bottom)]. For nanoimprinted samples, PC plays a similar role (Figure 6c).

We further analyze PC's effect by X-ray diffraction (XRD) measurements: after UV exposure, a specimen with PC exhibits the same crystallinity (Figure 6e) whereas one without PC shows significantly reduced crystallinity (Figure 6d). Figure 6f depicts a simplified schematic of the degradation mechanisms caused by heat, photon energy, oxygen, and moisture (top) and the isolation of the perovskite from the ambient atmosphere by PC encapsulation of pinholes and grain boundaries (bottom).

CONCLUSION

By directly patterning $MAPbBr_3$ into a 2D PhC cavity and encapsulating it with PC, we have demonstrated quasi-CW lasing from $MAPbBr_3$ up to 260 K, pumped with optical pulses of 17 ns duration and 355 nm wavelength. While comprehensively studying the temperature-dependent lasing behavior, we found a gradual increase of lasing threshold with temperature and better lasing performance when the cavity mode coincides with the thin film's resonance. By investigating $MAPbBr_3$ quality enhancement through NIL, we showed that NIL could reduce the number of inter- and intragranular

https://doi.org/10.1021/acsphotonics.2c00071
ACS Photonics 2022, 9, 1984−1991

defects and enlarge crystals, thus leading to smoother/flatter surfaces. We further showed that a thin layer of PC film could effectively encapsulate the remaining surface defects of $MAPbBr_3$ and protect devices from environmental hazards, resulting in long-term device stability. We expect that CW lasing from directly patterned perovskite cavities is within reach through the combined analysis of crystal quality, the degradation process during optical pumping, defect encapsulation, and laser performance.

EXPERIMENTAL SECTION AND METHODS

Atomic Resolution Scanning Transmission Electron Microscopy (STEM)/TEM. For atomic resolution imaging, aberration-corrected JEM-ARM 200F (JEOL USA Inc.) is employed at an accelerating voltage of 200 kV, which can be operated under either STEM mode or TEM mode. The morphology of the thin films before and after NIL is investigated using the STEM mode, and the atomic structure of nanoimprinted films is examined using the TEM mode. The sample thickness for STEM/TEM examination was reduced by scraping $MAPbBr_3$ thin films with a razor blade, and the scraped $MAPbBr_3$ is dispersed in toluene by ultrasonication for a few minutes. The resulting solution (toluene and scraped $MAPbBr_3$) is dropped on a TEM grid (Cu-300HD, copper grids, 300 mesh), and STEM/TEM is performed after the evaporation of toluene. For nanoimprinted samples, $MAPbBr_3$ films are imprinted with a flat stamp before being scraped with a razor blade. Note that although specimen preparation for TEM usually requires focused ion beam lithography to thin down the sample, the above approach is used to avoid damage during sample preparation.

X-ray Diffraction (XRD). XRD measurements are performed using a Rigaku SmartLab X-ray Cu target (Ka1 = 1.54059 Å) and a HyPix 3000 detector. Out of plane measurements (2-theta/omega scan) are performed on all samples under the same measurement conditions, in the 2-theta range of 5− 60° with 0.01° step and ∼2° per min scan speed, to see the thin film crystallinity and structure.

Atomic Force Microscopy (AFM). AFM images are taken using a Veeco Multimode V SPM to examine the morphology of thin films. The thin films are scanned for a 2 × 2 μm area at a 0.8 Hz rate using an AFM tip (OTESPA-R3 from Bruker).

Steady State Microphotoluminescence (Micro-PL) Spectroscopy. The device under test is excited with 17 ns optical pulses at 355 nm (TALON-355−20, Spectra-Physics), with a spot size of 100 μm in diameter. Emission from the sample is collected using a cascaded 4-f system and focused onto the slit of a spectrograph (Princeton Instruments, IsoPlane SCT-320) coupled to a cooled Si detector (Princeton Instruments, PIXIS:400BRX). A more detailed description can be found in Supplementary Part H.

ASSOCIATED CONTENT

Supporting Information

The Supporting Information is available free of charge at https://pubs.acs.org/doi/10.1021/acsphotonics.2c00071.

SEM images after key steps of the NIL stamp fabrication; SEM image of the stamp map and pictures of fabricated stamp, as-spin-coated $MAPbBr_3$ and $MAPbBr_3$ film after NIL; schematic and details of NIL process; SEM images of the pattern of the stamp, the imprinted pattern, and the PC-encapsulated imprinted pattern; schematic of the 2D PhC dimensions and thin film to calculate residue thickness; details in the simulated $MAPbBr_3$ PhC cavity; lasing threshold evolution plot as a function of temperature; PL and ASE of $MAPbBr_3$ after flat NIL at different temperatures; SEM images and PL of $MAPbBr_3$ before and after NIL; PL comparisons between $MAPbBr_3$ films with and without PC after five months; SEM image of photobleached PhC pattern without PC; SEM images of Al_2O_3-encapsulated $MAPbBr_3$ before and after UV; TEM images showing degradation under e-beam; TEM images of $MAPbBr_3$ without NIL; and details and schematic of the steady state micro-PL measurement setup (PDF)

AUTHOR INFORMATION

Corresponding Author

Qing Gu − *Department of Electrical and Computer Engineering, The University of Texas at Dallas, Richardson, Texas 75080, United States; Department of Electrical and Computer Engineering and Department of Physics, North Carolina State University, Raleigh, North Carolina 27695, United States;* orcid.org/0000-0003-3855-3690; Email: qgu3@ncsu.edu

Authors

Jiyoung Moon − *Department of Material Science and Engineering, The University of Texas at Dallas, Richardson, Texas 75080, United States*

Masoud Alahbakhshi − *Department of Electrical and Computer Engineering, The University of Texas at Dallas, Richardson, Texas 75080, United States*

Abouzar Gharajeh − *Department of Electrical and Computer Engineering, The University of Texas at Dallas, Richardson, Texas 75080, United States*

Quanwei Li − *Nanoscale Science and Engineering Center (NSEC), University of California, Berkeley, Berkeley, California 94720, United States*

Zhitong Li − *Department of Electrical and Computer Engineering, The University of Texas at Dallas, Richardson, Texas 75080, United States*

Ross Haroldson − *Department of Physics, The University of Texas at Dallas, Richardson, Texas 75080, United States*

Sunah Kwon − *Department of Material Science and Engineering, The University of Texas at Dallas, Richardson, Texas 75080, United States*

Roberta Hawkins − *Department of Material Science and Engineering, The University of Texas at Dallas, Richardson, Texas 75080, United States*

Moon J. Kim − *Department of Material Science and Engineering, The University of Texas at Dallas, Richardson, Texas 75080, United States;* orcid.org/0000-0002-2972-493X

Walter Hu − *Department of Electrical and Computer Engineering, The University of Texas at Dallas, Richardson, Texas 75080, United States*

Xiang Zhang − *Nanoscale Science and Engineering Center (NSEC), University of California, Berkeley, Berkeley, California 94720, United States; Faculty of Science and Faculty of Engineering, The University of Hong Kong, Hong Kong, China;* orcid.org/0000-0002-3272-894X

Anvar Zakhidov − *Department of Physics, The University of Texas at Dallas, Richardson, Texas 75080, United States;*

https://doi.org/10.1021/acsphotonics.2c00071
ACS Photonics 2022, 9, 1984−1991

Department of Nanophotonics and Metamaterials, ITMO University, St. Petersburg 197101, Russia

Complete contact information is available at: https://pubs.acs.org/10.1021/acsphotonics.2c00071

Author Contributions

[O]J.M., M.A., and A.G. contributed equally. Q.G., A.Z., and W.H. conceived the project idea. J.M. designed the experiments under the guidance of Q.G.; fabricated the NIL stamps; performed PC encapsulation; conducted XRD, SEM, and XPS measurements; and carried out the postprocessing of the optical and material characterization results. M.A. prepared the $MAPbBr_3$ solutions and thin films and performed NIL and PL measurements. A.G. built the micro-PL setup with a ns pump laser and performed PL measurements. Q.L. built the micro-PL setup with a fs pump laser and performed PL measurements. Z.L. performed optical simulations. R.Haroldson prepared and optimized the $MAPbBr_3$ solutions and spin-coating recipes. S.K. conducted STEM, TEM, and AFM measurements. R.Hawkins conducted NIL. J.M. and Q.G. wrote the manuscript. All authors participated in data analysis and the improvement of the manuscript.

Funding

This work is supported by the National Science Foundation (NSF) CAREER Award (ECCS-2209871), the Army Research Office (ARO) Young Investigator Program (W911NF-19−1−0303), the Texas Instruments Early Career Award, and the Welch Foundation (grant AT-1992−20190330 and AT-1617).

Notes

The authors declare no competing financial interest.

REFERENCES

(1) Zhou, Z.; Yin, B.; Michel, J. On-Chip Light Sources for Silicon Photonics. *Light: Science and Applications* **2015**, *4* (11), e358.

(2) Soltani, M.; Soref, R.; Palacios, T.; Englund, D. AlGaN/AlN Integrated Photonics Platform for the Ultraviolet and Visible Spectral Range. *Opt. Express* **2016**, *24* (22), 25415.

(3) Xiang, C.; Guo, J.; Jin, W.; Wu, L.; Peters, J.; Xie, W.; Chang, L.; Shen, B.; Wang, H.; Yang, Q. F.; Kinghorn, D.; Paniccia, M.; Vahala, K. J.; Morton, P. A.; Bowers, J. E. High-Performance Lasers for Fully Integrated Silicon Nitride Photonics. *Nat. Commun.* **2021**, *12* (1), 1−8.

(4) Wan, Y.; Zhang, S.; Norman, J. C.; Kennedy, M. J.; He, W.; Liu, S.; Xiang, C.; Shang, C.; He, J.-J.; Gossard, A. C.; Bowers, J. E. Tunable Quantum Dot Lasers Grown Directly on Silicon. *Optica* **2019**, *6* (11), 1394−1400.

(5) Duan, Z.; Wang, Y.; Li, G.; Wang, S.; Yi, N.; Liu, S.; Xiao, S.; Song, Q. Chip-Scale Fabrication of Uniform Lead Halide Perovskites Microlaser Array and Photodetector Array. *Laser and Photonics Reviews* **2018**, *12* (1), 1700234.

(6) Ren, K.; Wang, J.; Chen, S.; Yang, Q.; Tian, J.; Yu, H.; Sun, M.; Zhu, X.; Yue, S.; Sun, Y.; Liu, K.; Azam, M.; Wang, Z.; Jin, P.; Qu, S.; Wang, Z. Realization of Perovskite-Nanowire-Based Plasmonic Lasers Capable of Mode Modulation. *Laser and Photonics Reviews* **2019**, *13* (7), 1800306.

(7) Saba, M.; Cadelano, M.; Marongiu, D.; Chen, F.; Sarritzu, V.; Sestu, N.; Figus, C.; Aresti, M.; Piras, R.; Geddo Lehmann, A.; Cannas, C.; Musinu, A.; Quochi, F.; Mura, A.; Bongiovanni, G. Correlated Electron-Hole Plasma in Organometal Perovskites. *Nat. Commun.* **2014**, *5* (May), 1−10.

(8) Zhu, H.; Fu, Y.; Meng, F.; Wu, X.; Gong, Z.; Ding, Q.; Gustafsson, M. v.; Trinh, M. T.; Jin, S.; Zhu, X. Y. Lead Halide Perovskite Nanowire Lasers with Low Lasing Thresholds and High Quality Factors. *Nat. Mater.* **2015**, *14* (6), 636−642.

(9) Jia, Y.; Kerner, R. A.; Grede, A. J.; Rand, B. P.; Giebink, N. C. Continuous-Wave Lasing in an Organic-Inorganic Lead Halide Perovskite Semiconductor. *Nat. Photonics* **2017**, *11* (12), 784−788.

(10) Qin, C.; Sandanayaka, A. S. D.; Zhao, C.; Matsushima, T.; Zhang, D.; Fujihara, T.; Adachi, C. Stable Room-Temperature Continuous-Wave Lasing in Quasi-2D Perovskite Films. *Nature* **2020**, *585* (7823), 53−57.

(11) Bar-On, O.; Brenner, P.; Lemmer, U.; Scheuer, J. Micro Lasers by Scalable Lithography of Metal-Halide Perovskites. *Advanced Materials Technologies* **2018**, *3* (12), 1800212.

(12) Pourdavoud, N.; Mayer, A.; Buchmüller, M.; Brinkmann, K.; Häger, T.; Hu, T.; Heiderhoff, R.; Shutsko, I.; Görrn, P.; Chen, Y.; Scheer, H. C.; Riedl, T. Distributed Feedback Lasers Based on MAPbBr3. *Advanced Materials Technologies* **2018**, *3*, 1700253.

(13) Pourdavoud, N.; Haeger, T.; Mayer, A.; Cegielski, P. J.; Giesecke, A. L.; Heiderhoff, R.; Olthof, S.; Zaefferer, S.; Shutsko, I.; Henkel, A.; Becker-Koch, D.; Stein, M.; Cehovski, M.; Charfi, O.; Johannes, H. H.; Rogalla, D.; Lemme, M. C.; Koch, M.; Vaynzof, Y.; Meerholz, K.; Kowalsky, W.; Scheer, H. C.; Görrn, P.; Riedl, T. Room-Temperature Stimulated Emission and Lasing in Recrystallized Cesium Lead Bromide Perovskite Thin Films. *Adv. Mater.* **2019**, *31*, 1903717.

(14) Cegielski, P. J.; Giesecke, A. L.; Neutzner, S.; Porschatis, C.; Gandini, M.; Schall, D.; Perini, C. A. R.; Bolten, J.; Suckow, S.; Kataria, S.; Chmielak, B.; Wahlbrink, T.; Petrozza, A.; Lemme, M. C. Monolithically Integrated Perovskite Semiconductor Lasers on Silicon Photonic Chips by Scalable Top-Down Fabrication. *Nano Lett.* **2018**, *18* (11), 6915−6923.

(15) Huang, C.; Zhang, C.; Xiao, S.; Wang, Y.; Fan, Y.; Liu, Y.; Zhang, N.; Qu, G.; Ji, H.; Han, J.; Ge, L.; Kivshar, Y.; Song, Q. Ultrafast Control of Vortex Microlasers. *Science* **2020**, *367* (6481), 1018−1021.

(16) Wang, S.; Liu, Y.; Li, G.; Zhang, J.; Zhang, N.; Xiao, S.; Song, Q. Lead Halide Perovskite Based Microdisk Lasers for On-Chip Integrated Photonic Circuits. *Advanced Optical Materials* **2018**, *6*, 1701266.

(17) Xing, G.; Mathews, N.; Lim, S. S.; Yantara, N.; Liu, X.; Sabba, D.; Grätzel, M.; Mhaisalkar, S.; Sum, T. C. Low-Temperature Solution-Processed Wavelength-Tunable Perovskites for Lasing. *Nat. Mater.* **2014**, *13* (5), 476−480.

(18) Deschler, F.; Price, M.; Pathak, S.; Klintberg, L. E.; Jarausch, D. D.; Higler, R.; Hüttner, S.; Leijtens, T.; Stranks, S. D.; Snaith, H. J.; Atatüre, M.; Phillips, R. T.; Friend, R. H. High Photoluminescence Efficiency and Optically Pumped Lasing in Solution-Processed Mixed Halide Perovskite Semiconductors. *J. Phys. Chem. Lett.* **2014**, *5* (8), 1421−1426.

(19) Mi, Y.; Zhong, Y.; Zhang, Q.; Liu, X. Continuous-Wave Pumped Perovskite Lasers. *Advanced Optical Materials* **2019**, *7* (17), 1900544.

(20) Shang, Q.; Li, M.; Zhao, L.; Chen, D.; Zhang, S.; Chen, S.; Gao, P.; Shen, C.; Xing, J.; Xing, G.; Shen, B.; Liu, X.; Zhang, Q. Role of the Exciton-Polariton in a Continuous-Wave Optically Pumped CsPbBr3Perovskite Laser. *Nano Lett.* **2020**, *20* (9), 6636−6643.

(21) Zhang, Q.; Shang, Q.; Su, R.; Do, T. T. H.; Xiong, Q. Halide Perovskite Semiconductor Lasers: Materials, Cavity Design, and Low Threshold. *Nano Lett.* **2021**, *21* (5), 1903−1914.

(22) Das, S.; Gholipour, S.; Saliba, M. Perovskites for Laser and Detector Applications. *Energy Environ. Mater.* **2019**, *2*, 146−153.

(23) Yang, Y.; Yang, M.; Moore, D. T.; Yan, Y.; Miller, E. M.; Zhu, K.; Beard, M. C. Top and Bottom Surfaces Limit Carrier Lifetime in Lead Iodide Perovskite Films. *Nature Energy* **2017**, *2* (2), 1−7.

(24) Xing, G.; Mathews, N.; Sun, S.; Lim, S. S.; Lam, Y. M.; Gratzel, M.; Mhaisalkar, S.; Sum, T. C. Long-Range Balanced Electron- and Hole-Transport Lengths in Organic-Inorganic CH3NH3PbI3. *Science* **2013**, *342* (6156), 344−347.

(25) Kerner, R. A.; Rand, B. P. Ionic-Electronic Ambipolar Transport in Metal Halide Perovskites: Can Electronic Conductivity Limit Ionic Diffusion? *J. Phys. Chem. Lett.* **2018**, *9* (1), 132−137.

(26) de Quilettes, D. W.; Vorpahl, S. M.; Stranks, S. D.; Nagaoka, H.; Eperon, G. E.; Ziffer, M. E.; Snaith, H. J.; Ginger, D. S. Impact of Microstructure on Local Carrier Lifetime in Perovskite Solar Cells. *Science* **2015**, *348* (6235), 683−686.
(27) Li, Z.; Moon, J.; Gharajeh, A.; Haroldson, R.; Hawkins, R.; Hu, W.; Zakhidov, A.; Gu, Q. Roomerature Continuous-Wave Operation of Organometal Halide Perovskite Lasers. *ACS Nano* **2018**, *12* (11), 10968−10976.
(28) Samuel, I. D. W. W.; Namdas, E. B.; Turnbull, G. A. How to Recognize Lasing. *Nat. Photonics* **2009**, *3* (10), 546−549.
(29) Liu, Y.; Lu, H.; Niu, J.; Zhang, H.; Lou, S.; Gao, C.; Zhan, Y.; Zhang, X.; Jin, Q.; Zheng, L. Temperature-Dependent Photoluminescence Spectra and Decay Dynamics of MAPbBr3 and MAPbI3 Thin Films. *AIP Advances* **2018**, *8*, 095108.
(30) Lafalce, E.; Zhang, C.; Zhai, Y.; Sun, D.; Vardeny, Z. v. Enhanced Emissive and Lasing Characteristics of Nano-Crystalline MAPbBr3 Films Grown via Anti-Solvent Precipitation. *J. Appl. Phys.* **2016**, *120*, 143101.
(31) Sheng, R.; Wen, X.; Huang, S.; Hao, X.; Chen, S.; Jiang, Y.; Deng, X.; Green, M. A.; Ho-Baillie, A. W. Y. Photoluminescence Characterisations of a Dynamic Aging Process of Organic-Inorganic CH3NH3PbBr3 Perovskite. *Nanoscale* **2016**, *8* (4), 1926−1931.
(32) Pelton, M. Modified Spontaneous Emission in Nanophotonic Structures. *Nat. Photonics* **2015**, *9* (7), 427−435.
(33) Chen, S.; Roh, K.; Lee, J.; Chong, W. K.; Lu, Y.; Mathews, N.; Sum, T. C.; Nurmikko, A. A Photonic Crystal Laser from Solution Based Organo-Lead Iodide Perovskite Thin Films. *ACS Nano* **2016**, *10* (4), 3959−3967.
(34) D'Innocenzo, V.; Srimath Kandada, A. R.; de Bastiani, M.; Gandini, M.; Petrozza, A. Tuning the Light Emission Properties by Band Gap Engineering in Hybrid Lead Halide Perovskite. *J. Am. Chem. Soc.* **2014**, *136* (51), 17730−17733.
(35) de Giorgi, M. L.; Perulli, A.; Yantara, N.; Boix, P. P.; Anni, M. Amplified Spontaneous Emission Properties of Solution Processed $CsPbBr_3$ Perovskite Thin Films. *J. Phys. Chem. C* **2017**, *121* (27), 14772−14778.
(36) Gu, Q.; Smalley, J. S. T.; Shane, J.; Bondarenko, O.; Fainman, Y. Temperature Effects in Metal-Clad Semiconductor Nanolasers. *Nanophotonics* **2015**, *4* (1), 26−43.
(37) O'Gorman, J.; Levi, A. F. J.; Schmitt-Rink, S.; Tanbun-Ek, T.; Coblentz, D. L.; Logan, R. A. On the Temperature Sensitivity of Semiconductor Lasers. *Appl. Phys. Lett.* **1992**, *60* (2), 157−159.
(38) Varshni, Y. P. Temperature Dependence of the Energy Gap in Semiconductors. *Physica* **1967**, *34* (1), 149−154.
(39) Cho, C.; Palatnik, A.; Sudzius, M.; Grodofzig, R.; Nehm, F.; Leo, K. Controlling and Optimizing Amplified Spontaneous Emission in Perovskites. *ACS Appl. Mater. Interfaces* **2020**, *12* (31), 35242−35249.
(40) Brenner, P.; Bar-On, O.; Jakoby, M.; Allegro, I.; Richards, B. S.; Paetzold, U. W.; Howard, I. A.; Scheuer, J.; Lemmer, U. Continuous Wave Amplified Spontaneous Emission in Phase-Stable Lead Halide Perovskites. *Nat. Commun.* **2019**, *10* (1), 1−7.
(41) Moon, J.; Kwon, S.; Alahbakhshi, M.; Lee, Y.; Cho, K.; Zakhidov, A.; Kim, M. J.; Gu, Q. Surface Energy-Driven Preferential Grain Growth of Metal Halide Perovskites: Effects of Nanoimprint Lithography beyond Direct Patterning. *ACS Appl. Mater. Interfaces* **2021**, *13* (4), 5368−5378.
(42) Giesbrecht, N.; Schlipf, J.; Oesinghaus, L.; Binek, A.; Bein, T.; Müller-Buschbaum, P.; Docampo, P. Synthesis of Perfectly Oriented and Micrometer-Sized MAPbBr3Perovskite Crystals for Thin-Film Photovoltaic Applications. *ACS Energy Letters* **2016**, *1* (1), 150−154.
(43) Fu, L.; Li, H.; Wang, L.; Yin, R.; Li, B.; Yin, L. Defect Passivation Strategies in Perovskites for an Enhanced Photovoltaic Performance. *Energy Environ. Sci.* **2020**, *13* (11), 4017−4056.
(44) Noel, N. K.; Abate, A.; Stranks, S. D.; Parrott, E. S.; Burlakov, V. M.; Goriely, A.; Snaith, H. J. Enhanced Photoluminescence and Solar Cell Performance via Lewis Base Passivation of Organic-Inorganic Lead Halide Perovskites. *ACS Nano* **2014**, *8* (10), 9815−9821.
(45) Dong, X.; Fang, X.; Lv, M.; Lin, B.; Zhang, S.; Ding, J.; Yuan, N. Improvement of the Humidity Stability of Organic-Inorganic Perovskite Solar Cells Using Ultrathin Al2O3layers Prepared by Atomic Layer Deposition. *Journal of Materials Chemistry A* **2015**, *3* (10), 5360−5367.
(46) Lv, Y.; Xu, P.; Ren, G.; Chen, F.; Nan, H.; Liu, R.; Wang, D.; Tan, X.; Liu, X.; Zhang, H.; Chen, Z. K. Low-Temperature Atomic Layer Deposition of Metal Oxide Layers for Perovskite Solar Cells with High Efficiency and Stability under Harsh Environmental Conditions. *ACS Appl. Mater. Interfaces* **2018**, *10* (28), 23928−23937.
(47) Kus, P.; Albrecht, S.; Schmeisser, D.; Kot, M.; Matolin, V.; Kegelmann, L.; Das, C.; Tsud, N.; Matolinova, I. Room-Temperature Atomic-Layer-Deposited Al 2 O 3 Improves the Efficiency of Perovskite Solar Cells over Time. *ChemSusChem* **2018**, *11* (20), 3640−3648.
(48) Koushik, D.; Kuang, Y.; Verheijen, M. A.; Creatore, M.; Schropp, R. E. I.; Verhees, W. J. H.; Veenstra, S.; Zhang, D. High-Efficiency Humidity-Stable Planar Perovskite Solar Cells Based on Atomic Layer Architecture. *Energy Environ. Sci.* **2017**, *10* (1), 91−100.

https://doi.org/10.1021/acsphotonics.2c00071
ACS Photonics 2022, 9, 1984−1991